Evolution, Structure, Cloud Microphysical, and Surface Rainfall Processes of Monsoon Convection during the South China Sea Monsoon Experiment

JIAN-JIAN WANG

Goddard Center for Earth Science and Technology, University of Maryland, Baltimore County, Baltimore, and Mesoscale Atmospheric Processes Branch, NASA Goddard Space Flight Center, Greenbelt, Maryland

XIAOFAN LI

Joint Center for Satellite Data Assimilation, and NOAA/NESDIS/Center for Satellite Applications and Research, Camp Springs, Maryland

LAWRENCE D. CAREY

Department of Atmospheric Sciences, Texas A&M University, College Station, Texas

(Manuscript received 23 January 2006, in final form 12 June 2006)

ABSTRACT

A two-dimensional cloud-resolving simulation is combined with dual-Doppler and polarimetric radar analysis to study the evolution, dynamic structure, cloud microphysics, and rainfall processes of monsoon convection observed during the South China Sea (SCS) summer monsoon onset.

Overall, the model simulations show many similarities to the radar observations. The rainband associated with the convection remains at a very stable position throughout its life cycle in the northern SCS. The reflectivity pattern exhibits a straight upward structure with little tilt. The positions of the convective, transition, and stratiform regions produced by the model are consistent with the observations. The major difference from the observations is that the model tends to overestimate the magnitude of updraft. As a result, the maximum reflectivity generated by the model appears at an elevated altitude.

The surface rainfall processes and associated thermodynamic, dynamic, and cloud microphysical processes are examined by the model in terms of surface rainfall, temperature and moisture perturbations, circulations, and cloud microphysical budget. At the preformation and dissipating stages, although local vapor change and vapor convergence terms are the major contributors in determining rain rate, they cancel each other out and cause little rain. The vapor convergence/divergence is closely related to the lower-tropospheric updraft/subsidence during the early/late stages of the convection. During the formation and mature phases, vapor convergence term is in control of the rainfall processes. Meanwhile, water microphysical processes are dominant in these stages. The active vapor condensation process causes a large amount of raindrops through the collection of cloud water by raindrops. Ice microphysical processes including riming are negligible up to the mature phase but are dominant during the weakening stage. Cloud source/sink terms make some contributions to the rain rate at the formation and weakening stages, while the role of surface evaporation term is negligible throughout the life cycle of the convection.

1. Introduction

The East Asian monsoon is an important component of the regional and global climate. In summer, the moist air brought by the low-level southwesterly flow across the South China Sea (SCS) feeds convective systems over the eastern Asian countries including China, Japan, and Korea. The quasi-stationary rainbelt associated with the monsoon system, the so-called mei-yu in China and Baiu in Japan, has been studied for a variety of meteorological, hydrological, and agricultural purposes. Although the East Asian summer monsoon attracts more attention when it affects the land area to the north during June–August, the onset of the East Asian summer monsoon starts over the ocean to the

Corresponding author address: Dr. Jian-Jian Wang, Mesoscale Atmospheric Processes Branch, NASA Goddard Space Flight Center, Greenbelt, MD 20771.
E-mail: jjwang@agnes.gsfc.nasa.gov

DOI: 10.1175/JAS3852.1

© 2007 American Meteorological Society

south in the SCS region in May (Tao and Chen 1987). During May–June 1998, the South China Sea Monsoon Experiment (SCSMEX; Lau et al. 2000), an international field experiment to support the Tropical Rainfall Measuring Mission (TRMM; Simpson 1988), was conducted in the SCS and its surrounding areas. The main objectives of the experiment were to investigate the key physical mechanisms responsible for the onset and evolution of the summer monsoon, and to better understand dynamic and microphysical aspects of the precipitation systems associated with the monsoon.

Prior to the SCSMEX, due to the lack of a detailed observational network, most studies on the East Asian summer monsoon focused on planetary-scale phenomena and frontal systems over the land in the mid- to late stages of monsoon season. However, little attention has been given to the flow pattern change in the monsoon onset period and the evolution and development of the precipitation systems over the ocean in the early stages of monsoon. The comprehensive dataset collected during the SCSMEX provides a good opportunity to extend our knowledge in these areas. Recently, mainly using the SCSMEX sounding data, Chan et al. (2000), Ding and Liu (2001), Lau et al. (2002), and Johnson and Ciesielski (2002) have reported the large-scale and regional characteristics of the flow transition associated with the monsoon onset during the SCSMEX.

In 1998, the SCS summer monsoon onset included three steps (Ding and Liu 2001): 1) the low-level southwesterly winds from the Tropics prevailed in the northern SCS starting on 15 May, 2) the southwesterly monsoon flow at low levels spread to the whole SCS by 20 May, and 3) the upper-level northeasterly winds were established over the SCS region by 23–24 May. Johnson et al. (2005) found that there was a wide range of organization modes of convection over the northern SCS during the onset period. The model simulation by Tao et al. (2003) suggested that the two main types of organized convective systems, unicell (onset phase of monsoon) and multicell (mature phase of monsoon) are determined by the unidirectional and reverse wind shear profiles, respectively, above the midlevels. Using SCSMEX radar data, Wang (2004) and Wang and Carey (2005) performed detailed studies on a frontal case on 15 May in the early onset period and a squall-line case on 24 May in the late onset period, respectively. The evolution and structure of mesoscale precipitation systems observed during the early summer monsoon season have been documented in detail. Polarimetric radar inferred microphysical (e.g., hydrometeor type, amount, and size) and rainfall properties are placed in the context of the mesoscale morphology and dual-Doppler derived kinematics for this squall-line system. It is found that precipitation over the SCS monsoon region during the summer monsoon onset was quite similar to the precipitation over the Amazon monsoon region during the westerly regime of the TRMM Large-Scale Biosphere–Atmosphere experiment (LBA), which has previously been found to be closer to typical conditions over tropical oceans (e.g., Cifelli et al. 2002).

However, due to the limitation of radar observation, the previous studies on the monsoon convection during the early monsoon season only focused on the rainfall and airflow pattern along with microphysical properties. Although some reasonable speculations were derived from observational studies, the complete dynamic and thermodynamic mechanisms responsible for the rainfall processes are not fully understood. Tao et al. (2003) conducted a comparison study between observations and simulations using the domain-mean data during SCSMEX. Due to the scarcity of observational data, the comparison of small-scale (~a few kilometers) horizontal structures of convection has seldom been carried out. In this study, a comparison will be conducted between observed and modeled radar reflectivity, hydrometeor types, and circulations using radar data available during SCSMEX and a two-dimensional (2D) cloud-resolving simulation. After validation by radar observations, the 2D simulation data are further used to study life cycles of convection in terms of dynamic, thermodynamic, rainfall, and cloud microphysical analyses. In the next section, the data analysis procedures and model design will be briefly described. In section 3, the comparison between the simulations and observations are discussed. In section 4, surface rainfall processes, cloud microphysical processes, and associated vertical structures of temperature, vapor, and circulation are discussed with the analysis of the simulation data. A summary is given in section 5.

2. Data analysis and model design

a. Data process and analysis

The main observational data used in this study are the sounding data from the SCSMEX sounding network and the radar data collected from a ground-based and a shipborne radar. The additional sources of information also include *Geosynchronous Meteorological Satellite-5* (*GMS-5*) imagery, and the National Aeronautics and Space Administration (NASA) TRMM Microwave Image (TMI) radiometer data.

During May–June 1998, a sounding network was established in the SCS and its surrounding areas. In the vicinity of the SCS, the sounding frequency and resolution were the highest, with up to 4 launches day^{-1} and

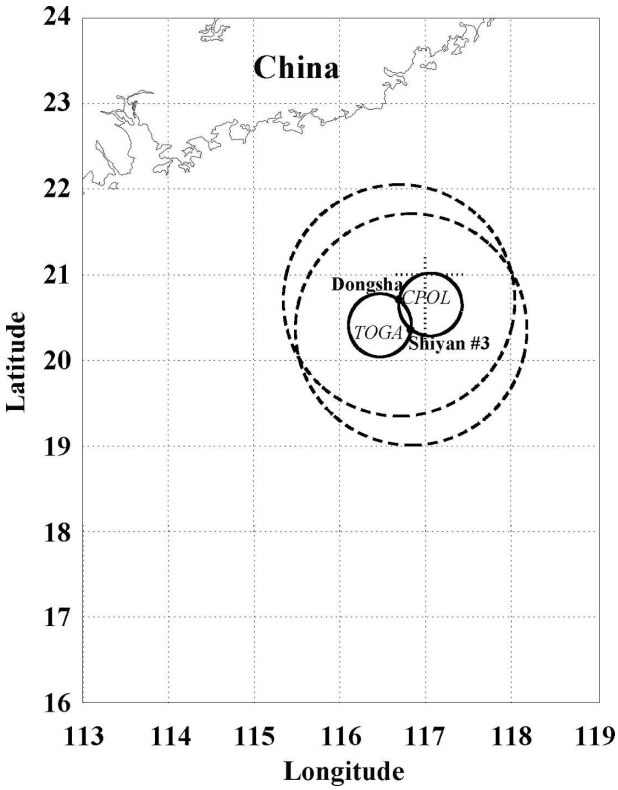

FIG. 1. Dual-Doppler radar network over the SCS during SCSMEX. The big dashed circles indicate the radar-observing domain, while the small solid circles show the dual-Doppler radar analysis regime.

5-hPa vertical resolution. Sounding quality control procedures were performed and documented by Johnson and Ciesielski (2002). They also computed gridded fields of horizontal components, temperature, specific humidity, and geopotential height at 1° resolution over the area covering 10°S–40°N, 80°–130°E. In this study, these gridded fields are used to initiate the cloud-resolving model.

During SCSMEX, the National Oceanographic and Atmospheric Administration (NOAA)/Tropical Ocean Global Atmosphere (TOGA) radar was installed on the People's Republic of China *Shiyan-3* research vessel (about 20.4°N, 116.8°E) and operated continuously during 5–25 May and 5–25 June, and Bureau of Meteorology Research Centre (BMRC, Australia) polarimetric C-POL radar was installed at Dongsha Island (20.7°N, 116.7°E) and operated on a 24-h basis (with several short breaks) throughout May and June 1998 (Fig. 1). A more detailed description of the issues related to radar data quality control and dual-Doppler radar analysis procedure was given by Wang (2004). In brief, due to a misaligned bandpass filter on the TOGA radar, the reflectivity (Z_H) measured by the TOGA was significantly biased. Therefore, only the reflectivity data collected from C-POL will be used in this study. In addition, due to the poor sensitivity of TOGA radar in the upper levels with weak reflectivity, it is difficult to define the upper boundary condition. Therefore, the upward integration method, instead of the better variational or downward integration methods, was used to calculate the vertical air motion. As found from error estimation (Wang 2004), the derived vertical velocities may not be reliable in the upper regions. Thus, no conclusion will be made from the derived vertical velocities at high levels.

In addition to the dual-Doppler radar analysis, a set of polarimetric variables were also available from C-POL including differential reflectivity (Z_{DR}), total differential phase (Ψ_{DP}), and zero lag correlation coefficient between copolar horizontal and vertical polarized electromagnetic waves (ρ_{HV}). An analysis of polarimetric radar-derived precipitation characteristics, including precipitation ice and liquid water content, was conducted using procedures similar to those outlined in Wang and Carey (2005). As described in earlier studies (Carey and Rutledge 2000; Cifelli et al. 2002), a difference reflectivity (Z_{DP}) method (Golestani et al. 1989) was used to estimate the horizontally polarized reflectivity (Z_H) for both rain and ice separately. The Z_H^{rain} was estimated directly from observations of Z_{DP}, and Z_H^{ice} was then estimated as a residual (i.e., $Z_H^{\mathrm{ice}} = Z_H^{\mathrm{observed}} - Z_H^{\mathrm{rain}}$). If the Z_{DP}-based method indicates the presence of mixed phase precipitation, then estimates of rainwater content (M_W, g m^{-3}) and ice water content (M_{ICE}, g m^{-3}) are calculated using equations:

$$M_W = 3.44 \times 10^{-3}[Z_H^{\mathrm{rain}}]^{4/7}(\mathrm{g\ m^{-3}}), \tag{1}$$

$$M_{\mathrm{ICE}} = 1000\,\pi\rho_i N_0^{3/7}\left(\frac{5.28 \times 10^{-18} Z_H^{\mathrm{ice}}}{720}\right)^{4/7} (\mathrm{g\ m^{-3}}), \tag{2}$$

where Z_H^{rain} and Z_H^{ice} are in mm^6 m^{-3}, ρ_{i} is the ice density (917 kg m^{-3}), and N_0 (4×10^6 m^{-4}) is the intercept parameter of an assumed inverse exponential distribution for ice. Note that Rayleigh scattering conditions are assumed. If the Z_{DP}-based method indicates the presence of pure rain (i.e., if the difference between observed Z_H and the estimated reflectivity associated with pure rain is less than the standard error, 0.9 dB), then it is assumed that the observed Z_H is dominated by water and the following equation from Bringi and Chandrasekar (2001) is utilized for estimating rainwater

$$M_W = 0.60 \times 10^{-3}(Z_H^{0.85})(\zeta^{-2.36}), \tag{3}$$

TABLE 1. List of microphysical processes and their parameterization schemes used in the cloud-resolving model. The schemes are Rutledge and Hobbs (1983; RH83), Rutledge and Hobbs (1984; RH84), Lin et al. (1983; LFO), Tao et al. (1989; TSM), and Krueger et al. (1995; KFLC).

Notation	Description	Scheme
P_{MLTG}	Growth of vapor by evaporation of liquid from graupel surface	RH84
P_{MLTS}	Growth of vapor by evaporation of melting snow	RH83
P_{REVP}	Growth of vapor by evaporation of raindrops	RH83
P_{IMLT}	Growth of cloud water by melting of cloud ice	RH83
P_{CND}	Growth of cloud water by the condensation of supersaturated vapor	TSM
P_{GMLT}	Growth of raindrops by melting of graupel	RH84
P_{SMLT}	Growth of raindrops by melting of snow	RH83
P_{RACI}	Growth of raindrops by the accretion of cloud ice	RH84
P_{RACW}	Growth of raindrops by the collection of cloud water	RH83
P_{RACS}	Growth of raindrops by the accretion of snow	RH84
P_{RAUT}	Growth of raindrops by the autoconversion of cloud water	LFO
P_{IDW}	Growth of cloud ice by the deposition of cloud water	KFLC
P_{IACR}	Growth of cloud ice by the accretion of rain	RH84
P_{IHOM}	Growth of cloud ice by the homogeneous freezing of cloud water	
P_{DEP}	Growth of cloud ice by the deposition of supersaturated vapor	TSM
P_{SAUT}	Growth of snow by the conversion of cloud ice	RH83
P_{SACI}	Growth of snow by the collection of cloud ice	RH83
P_{SACW}	Growth of snow by the accretion of cloud water	RH83
P_{SFW}	Growth of snow by the deposition and riming of cloud water	KFLC
P_{SFI}	Depositional growth of snow from cloud ice	KFLC
P_{SACR}	Growth of snow by the accretion of raindrops	LFO
P_{SDEP}	Growth of snow by the deposition of vapor	RH83
P_{GACI}	Growth of graupel by the collection of cloud ice	RH84
P_{GACR}	Growth of graupel by the accretion of raindrops	RH84
P_{GACS}	Growth of graupel by the accretion of snow	RH84
P_{GACW}	Growth of graupel by the accretion of cloud water	RH84
P_{WACS}	Growth of graupel by the riming of snow	RH84
P_{GDEP}	Growth of graupel by the deposition of vapor	RH84
P_{GFR}	Growth of graupel by the freezing of raindrops	LFO

where $\zeta = 10^{(Z_{\mathrm{DR}}/10)}$. When required in pure rain, raindrop size (i.e., mass weighted mean diameter, D_m) was estimated using Z_{DR} according to (Bringi and Chandrasekar 2001)

$$D_m = 1.619(Z_{\mathrm{DR}})^{0.485}\ (\mathrm{mm}). \tag{4}$$

If the Z_{DP}-based method indicates the presence of pure ice, then Eq. (2) is utilized, assuming $Z_H^{\mathrm{ice}} = Z_H$. As discussed in Carey and Rutledge (2000), the liquid and especially ice water contents reported herein are only approximate, since a number of assumptions were required.

b. Model and experiment design

The cloud-resolving model used in this study was originally developed by Soong and Ogura (1980), Soong and Tao (1980), and Tao and Simpson (1993). The 2D version of the model used by Sui et al. (1994, 1998) and further modified by Li et al. (1999) is what is used in this study. The governing equations and model setup can be found in Li et al. (1999, 2002a). The model includes five prognostic equations for mixing ratios of cloud water, raindrop, cloud ice, snow, and graupel. The cloud microphysical parameterization schemes (see Table 1) used in the model (Li et al. 1999, 2002a) are from Rutledge and Hobbs (1983, 1984), Lin et al. (1983), Tao et al. (1989), and Krueger et al. (1995). The model also includes solar (Chou et al. 1998) and thermal infrared (Chou et al. 1991; Chou and Suarez 1994) radiation parameterization schemes that are performed every 3 min. Cyclic lateral boundaries are used. The horizontal domain is 768 km with a horizontal grid resolution of 1.5 km. The top model level is 21 km. The vertical grid resolution ranges from about 200 m near the surface to about 1 km near 16 km. The time step is 12 s. Zonal-mean simulation data at hourly intervals are used in the following analysis. The cloud-resolving simulations have been validated with observations in terms of atmospheric thermodynamic profiles, surface fluxes, and surface rain rate in the Tropics during the Global Atmospheric Research Program (GARP) Atlantic Tropical Experiment (GATE; e.g., Xu and Randall 1996; Grabowski et al. 1996) and TOGA Coupled Ocean–Atmosphere Response Experiment (COARE;

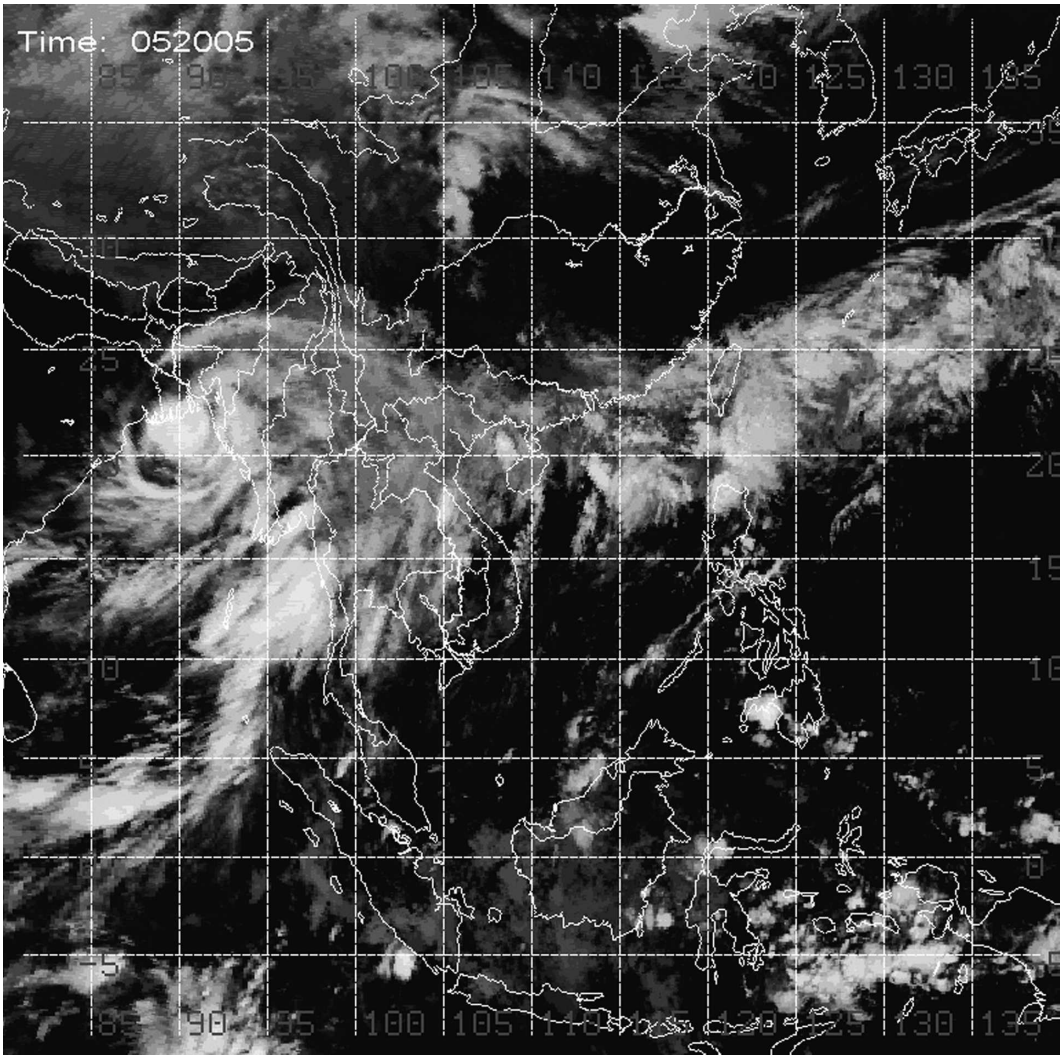

FIG. 2. Infrared imagery from *GMS-5* at 0500 LST 20 May 1998.

e.g., Wu et al. 1998; Li et al. 1999, 2002a,b; Gao et al. 2004, 2005a,b).

Based on the observation of the C-POL radar reflectivity (details later), we choose the area of 16°–23°N, 116°–117°E as the model simulation domain, and the forcing data are calculated accordingly. The model is forced by meridional-uniform vertical velocity, meridional wind, along with thermal and moisture advection. The forcing is averaged over the chosen area using 6-hourly observational data from the SCSMEX Intensive Observing Period (Johnson and Ciesielski 2002). Daily-mean sea surface temperature (SST) data are retrieved from the NASA TMI radiometer with a 10.7-GHz channel (Wentz et al. 2000), which is also imposed in the model. The model is integrated from 0200 local standard time (LST; LST = UTC + 0800) 20 May to 1400 LST 24 May 1998 (4.5 days total).

3. Comparison between simulations and observations

a. Synoptic conditions

The satellite infrared image for 0500 LST 20 May (Fig. 2) revealed that the northern SCS region was affected by two synoptic systems: a frontal system spreading from northern SCS to the south of Japan and a tropical cyclone in the Bay of Bengal and Indochina regions. Since the beginning of the summer monsoon onset on 15 May, frontal passages from northwestern China had affected the northern SCS region periodically with an interval of every 2–4 days. The observed tropical cyclone was formed in the Bay on Bengal on 17 May and slowly moved northeastward. The tropical cyclone brought more warm and moist air from the Tropics and also helped the progression of summer monsoon

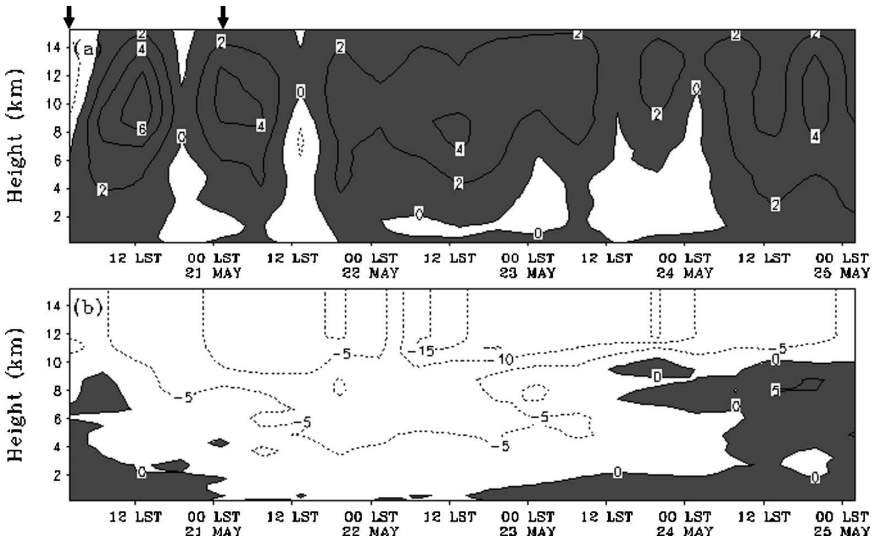

FIG. 3. Temporal and vertical distribution of (a) vertical velocity (cm s^{-1}) and (b) meridional wind (m s^{-1}) during selected SCSMEX period. Upward motion in (a) and southerly wind in (b) are shaded. The arrows above (a) indicate the analysis period in this study.

onset. The combined influences of these two synoptic systems made 19–20 May one of the rainiest day during the SCSMEX.

Figure 3 shows the time evolution of the vertical distribution of the large-scale vertical velocity and meridional wind, which are imposed in the model during the integrations. Since data from 0200 LST 20 May to 0200 LST 21 May 1998 are analyzed in this study, initialization of the model on 18 or 19 May is preferable. However, observational analysis shows constant downward motion during 18–19 May. The downward motion imposed in the cloud-resolving model will cause an unrealistic warming. Therefore 20 May 1998 is used as the model starting date when upward motion starts. Downward motion occurs in the early morning on 20 May 1998, followed by the strong upward motion around early afternoon on 20 May. The upward motion continues to dominate the rest of the integration period, while they are briefly interrupted by a few downward events, in particular, in the mid- and lower troposphere. The southerly winds start to diminish with the intensified northerly winds, which propagate downward. The southerly winds regain some strength in the mid- and lower troposphere on the last day of the integration period, although the northerly winds remain strong in the upper troposphere.

b. The evolution of the mesoscale convection

The frontal precipitation system moved into the SCSMEX radar observation domain in the early hours of 20 May. At 0430 LST, the dominant feature was an east–west-oriented rainband located to the north of the C-POL radar (Fig. 4a). The convection experienced a significant enhancement in intensity and areal coverage over the next 6 h (Figs. 4b,c). At 0800 LST, the most active portion of convection was in the left half of the dual-Doppler radar analysis domain. The leading edge of the system along with the convective rain was located to the south, followed by the stratiform rain to the north (Fig. 4c). A radar reflectivity of 55 dBZ was also recorded at 1.5 km MSL at this time. The dynamic and microphysical features of this part of the convection derived from dual-Doppler and polarimetric radar analysis will be presented in more detail later. After 0830 LST, the whole convective system remained at a similar strength with very slow propagation to the west. Despite the explosive development from 0200 to 1200 LST, the position of the rainband during this period was very stable, especially in the north–south direction. There were more secondary rainbands, also with an east–west orientation, formatting in the area near the main rainband at 1200 LST (Fig. 4d). At this point, the rainband also reached its peak areal extent. The intensity and size of the whole rainband were stable in the following hours with periodical reinforcement of the convective region on the southern edge. The rainband started to weaken at about 1700 LST and finally dissipated near 2300 LST (not shown).

Figure 5 displays the time evolution of the meridional distribution of the simulated surface rain rate. In the early morning on 20 May 1998, clouds formed in dif-

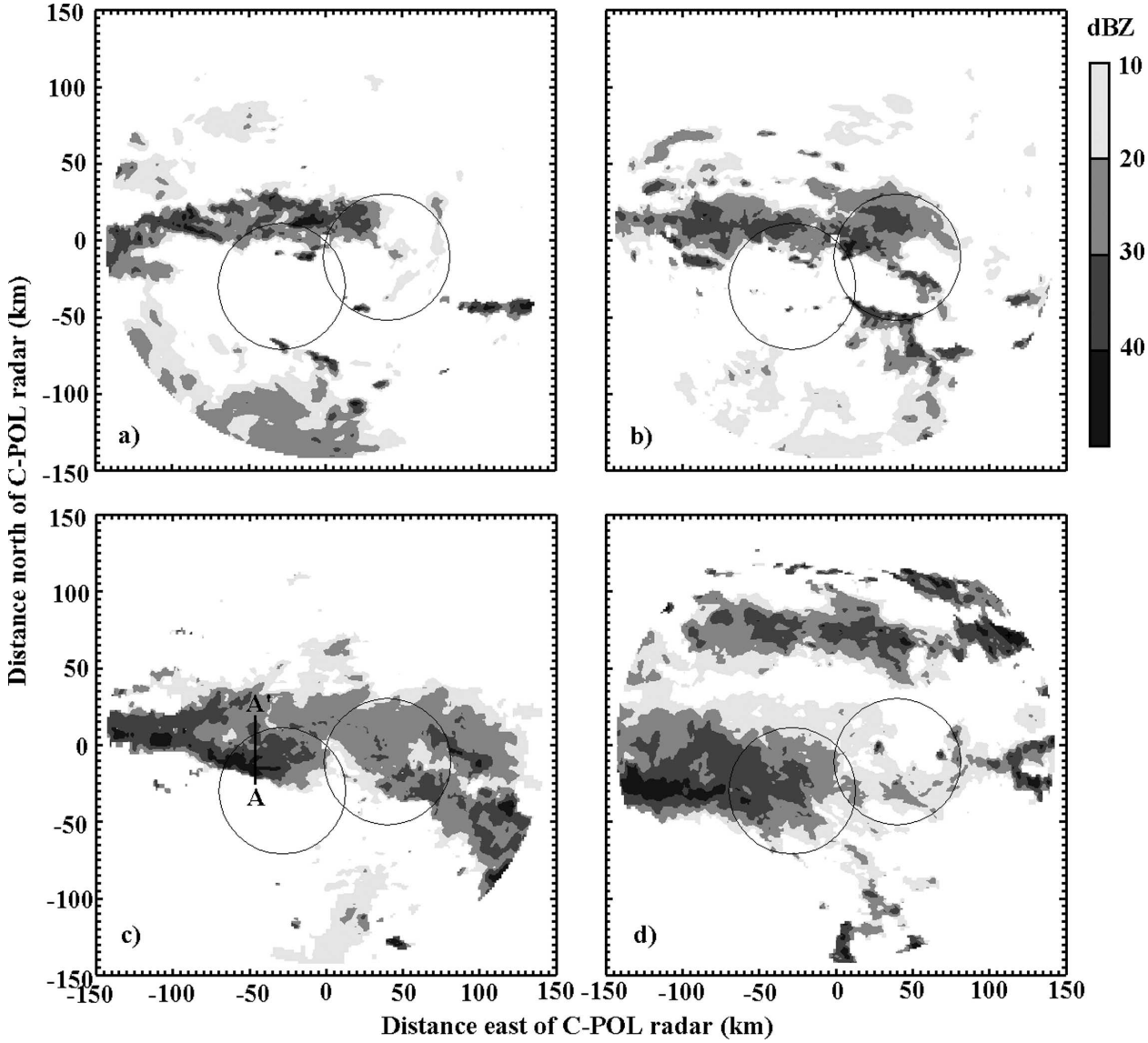

FIG. 4. The C-POL radar reflectivity (dBZ) at 2.5 km MSL at (a) 0430, (b) 0600, (c) 0800, and (d) 1200 LST 20 May 1998.

ferent locations, and three major rainbands appeared between 450 and 700 km. The rainbands barely moved, which is consistent with the observation in Fig. 4, while they intensified in the first 10 h of the integration. The stationary rainbands are due to the nearly zero layer-mean meridional wind resulting from the upper-tropospheric northerly winds and mid- and lower-tropospheric southerly winds (see Fig. 3). In the afternoon, the cloud clusters reached their maximum strength, as the imposed upward motion was at a maximum, while they propagated southward slightly as a result of the strengthening of imposed northerly winds. The clouds weakened when the imposed circulation became weak downward.

c. *The dynamic structure of the convection*

At 0800 LST, the main portion of the frontal rainband moved to the west of the C-POL and TOGA radars, an ideal location for a detailed dual-Doppler radar analysis. A vertical cross section through the convective complex is shown in Fig. 6 to characterize the rainfall pattern and the structure of air circulation. The reflectivity pattern was straight upward with little tilt, similar to other monsoon convections observed during monsoon onset as a result of weak vertical wind shear throughout the period (Wang 2004; Wang and Carey 2005). The convection was at its mature phase with the maximum radar reflectivity at about 55 DBZ and an echo top near 15 km MSL. There was a rapid reduction

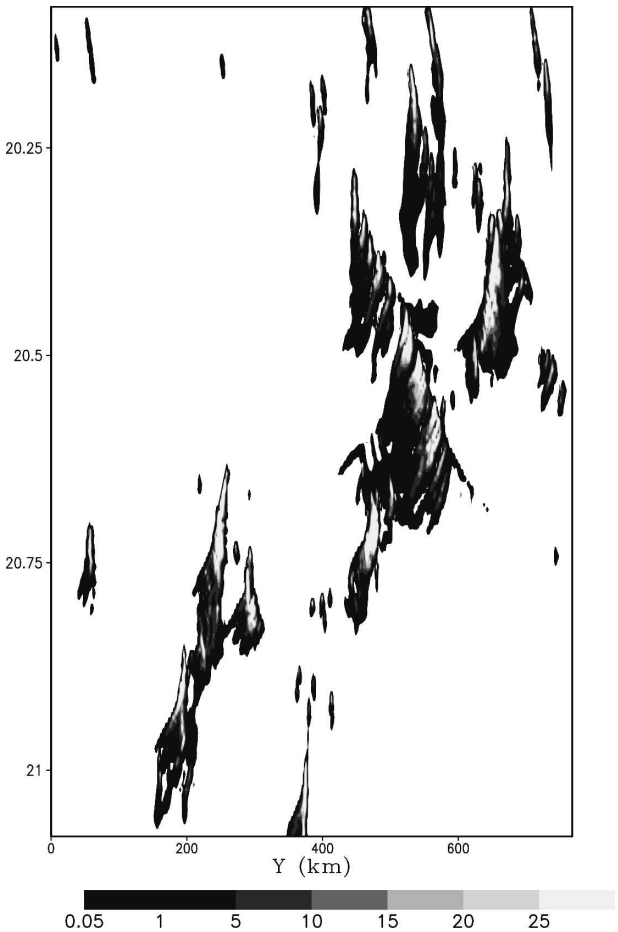

FIG. 5. Temporal and meridional distribution of simulated surface rain rate (mm h^{-1}).

in reflectivity with height above the melting level (~4.5 km MSL) as a result of relatively weak updraft velocities in most tropical oceanic convection (Zipser and LeMone 1980). The airflow pattern contains some common characteristics of tropical oceanic convection. The low-level inflow was from the warm and moist tropical air ahead of the leading edge. The center of the updraft was collocated with the convective core. There was a transition zone with weak radar reflectivity, generated by convective downward motion just behind the convective core. Following the transition zone, a stratiform rain echo, characterized by a radar reflectivity "bright band" (35–40 dBZ) near the melting layer, was located in the rear portion of the system. However, it is also noted that the size and shape of the low-level updraft zone observed herein were different from those documented for other tropical regions [e.g., the western Pacific (Jorgensen et al. 1997), and the Atlantic (Houze 1977)]. Usually, as a result of the convergence between incoming low-level flow and the outflow caused by the convection produced cold pool, the updraft zone is limited to a narrow ribbon-shaped area near the leading edge. However, the updraft of this system was in a wider region with a maxima extending to the rear part of the convective core. This atypical updraft pattern was also found in other SCSMEX convective systems and is likely related to the presence of a weak cold pool generated by the convection (Wang and Carey 2005).

To compare the model simulation to radar observation, the model-calculated hydrometeor density needs to be converted into the effective radar reflectivity [z_e (dBZ)], a parameter measured by the C-POL radar. The reflectivity factor (z) can be expressed by

$$z = \Gamma(7)\left(\frac{n_{0r}}{\lambda_r^7} + \frac{n_{0s}}{\lambda_s^7} + \frac{n_{0g}}{\lambda_g^7}\right), \tag{5}$$

where Γ is a Gamma function; n_{0r}, n_{0s}, and n_{0g} are the intercept values of raindrop, snow, and graupel size distributions, respectively; and λ_r, λ_s, and λ_g are the slopes of raindrop, snow, and graupel size distribution, respectively.

Considering the different dielectric fraction of water and other hydrometeor (e.g., ice), the effective reflectivity factor (z_e) can be calculated by

$$z_e = \frac{|K_x|^2}{|K_w|^2} z, \tag{6}$$

where $|K_w|^2 = 0.93$, is the dielectric fraction of water, and $|K_x|^2$ is the dielectric fraction of other hydrometeor (e.g., $|K_{\mathrm{ice}}|^2 = 0.176$ for equivalent ice spheres).

Then, the effective radar reflectivity (Z_e) can be calculated by

$$Z_e = 10 \log_{10}(z_e). \tag{7}$$

The convection simulated by the model (Fig. 7) reaches its mature phase at around 0900 LST, about an hour later than the radar observation. Therefore, the simulated reflectivity and wind vectors at 0900 LST (Fig. 7c) are compared to radar observations at 0800 LST (Fig. 6). The similarities between the simulation and observation include the following: 1) the reflectivity pattern is straight upward, 2) there is a wide updraft zone behind the leading edge, 3) the maximum ascending motion is associated with maximum reflectivity, 4) there are brightband reflectivity centers around the melting level behind the convective portion, and 5) there is a transition zone with weak reflectivity between the convective and stratiform rain center. Our simulation also confirmed the speculation of Wang and Carey (2005) that the cold pool generated by the early monsoon convection is relatively weak (less than 1°C shown in Fig. 12g). However, due to the nature of the 2D cloud

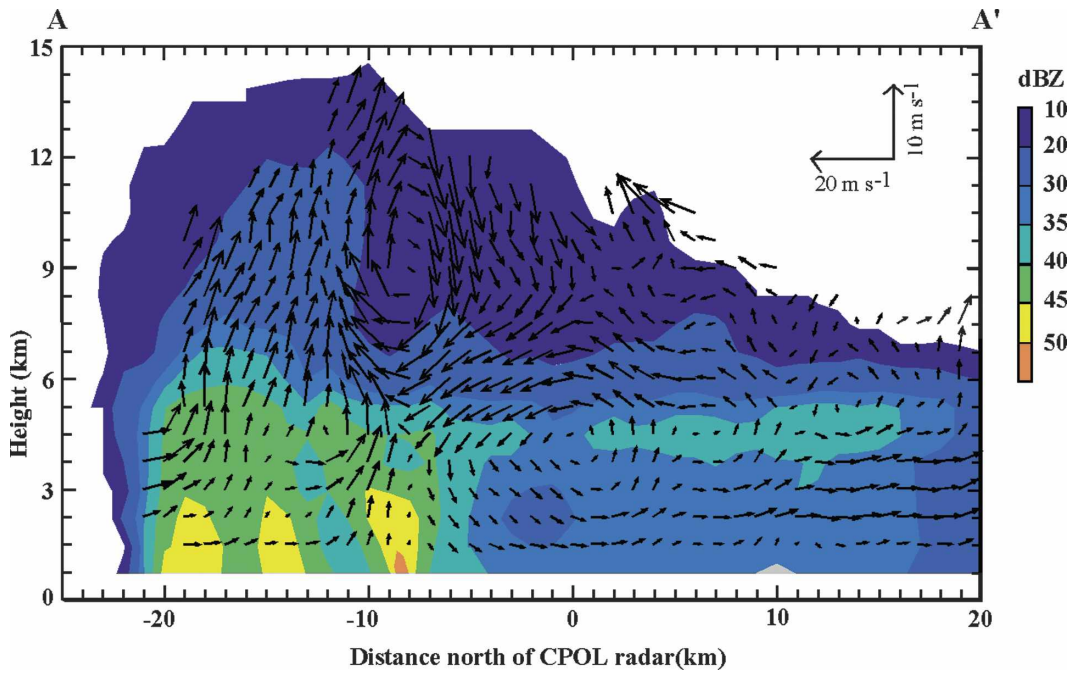

FIG. 6. Meridional–vertical (y–z) cross section of radar reflectivity (shaded) and system-relative wind flow (arrow vector) along line A–A′ shown in Fig. 4 at 0800 LST 20 May 1998 from observations.

model and the limitation of radar analysis, differences from the simulation to the observation are also evident. The simulation displays a maximum updraft of about 10 m s^{-1} at the midlevels. This could be an overestimation, as it is stronger than not only the radar estimation (5–6 m s^{-1} in Fig. 6), but also the observations of most tropical oceanic convection (Zipser and LeMone 1980; Jorgensen and LeMone 1989). This overestimation may also contribute to the maximum reflectivity at an elevated altitude (4–7 km). The radar data show a maximum radar reflectivity below 3 km MSL. This is typical for tropical oceanic convection because of the weak updraft. The other major difference is that the model-simulated updraft reduces rapidly above 9 km while the radar-derived updraft remains almost the same above 9 km in the convective core. As discussed before in section 2, limited by the missing TOGA radar data at the high levels, the upward integration has to be used for the computation of radar-derived vertical motion. This method may result in significant biases at the high levels (showing an apparent overestimation here) due to the error accumulations.

d. Rainfall and hydrometeor characteristics

Figure 8a shows a vertical cross section of differential reflectivity (Z_{DR}), a useful parameter to estimate the size of raindrops. The maximum Z_{DR} reached about 2.9 dB at the lowest levels close to the leading edge of the convection. That corresponded to drops of about 2.7 mm in diameter. However, even with a maximum Z_{DR} of 2.9 dB, the contour of 1 dB had a very small area coverage and was limited to below 3 km, well below the 0°C level. This indicated that oblate drops with diameter over 1.5 mm immediately fell out and were not lofted into the mixed phase region because of relatively weak updrafts at low levels. The midsized raindrops indicated by Z_{DR} of 0.5–1.0 dB in the convective part reached the level of 5.5–6 km. When the midsized drops were lofted to midlevels, they followed the updraft track and then were slowly sorted out by size toward the rear of the convection. Elevated Z_{DR} (>0.5 dB) collocated with low Z_H (<30 dBZ) at heights of 6 km and higher in the trailing anvil region were likely associated with horizontally oriented ice crystals or aggregates of ice crystals.

The representative cross section of rainwater content for the intense cell (Fig. 8b) exhibited maximum water content of over 4 g m^{-3} at the lowest 1.5-km level, collocated with the maximum reflectivity but behind the maximum Z_{DR}. This indicated that it was the small raindrops with D_m less than 1.5 mm at low levels that contributed to the maximum rainwater content in the convective core. Given the weak updrafts at 3–5 km MSL, the lofting of raindrops above the freezing level in the developing convection was negligible. As a result, there is very little precipitation ice mass in the system.

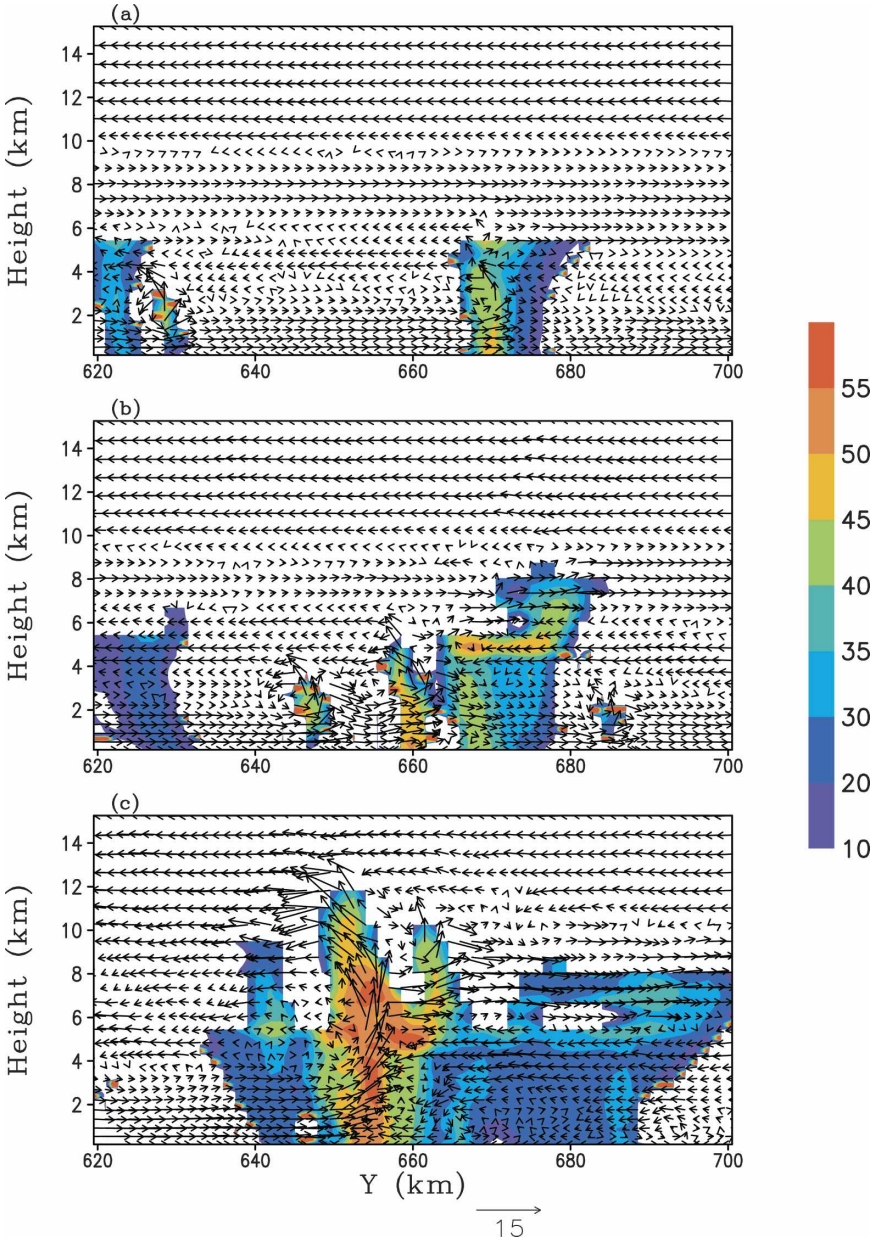

FIG. 7. Model-derived meridional–vertical (y–z) cross sections of reflectivity (dBZ) and wind vectors (m s^{-1}) at (a) 0700, (b) 0800, and (c) 0900 LST 20 May 1998.

The lack of significant raindrop freezing also denied the extra buoyancy that is contributed by latent heat release of freezing to the growing cells.

Figure 9 displays a meridional and vertical cross sections of hydrometeor density from 0700 to 0900 LST 20 May at 1-h intervals. At 0700 LST, three clouds appear around 620, 628, and 670 km. Hydrometeors associated with all three clouds limit to 5–6 km, indicating water clouds. At 0800 LST, hydrometeors around 670 km extend to 7 km while it elongates north, showing an ice-dominated anvil cloud. The formation of the anvil cloud also marks the mature stage of the convection. At 0900 LST, the convection with the anvil cloud around 665 km dissipates, while the convection around 655 km grows significantly, with the hydrometeors extending up to 12 km. The hydrometeor density over 4 g m^{-3} extended from the surface to 4 km with the maxima reaching 6 g m^{-3}. The simulated hydrometeor density at 0900 LST is compared with the observed density at 0800 LST (Fig. 8b). Both simulation and observation

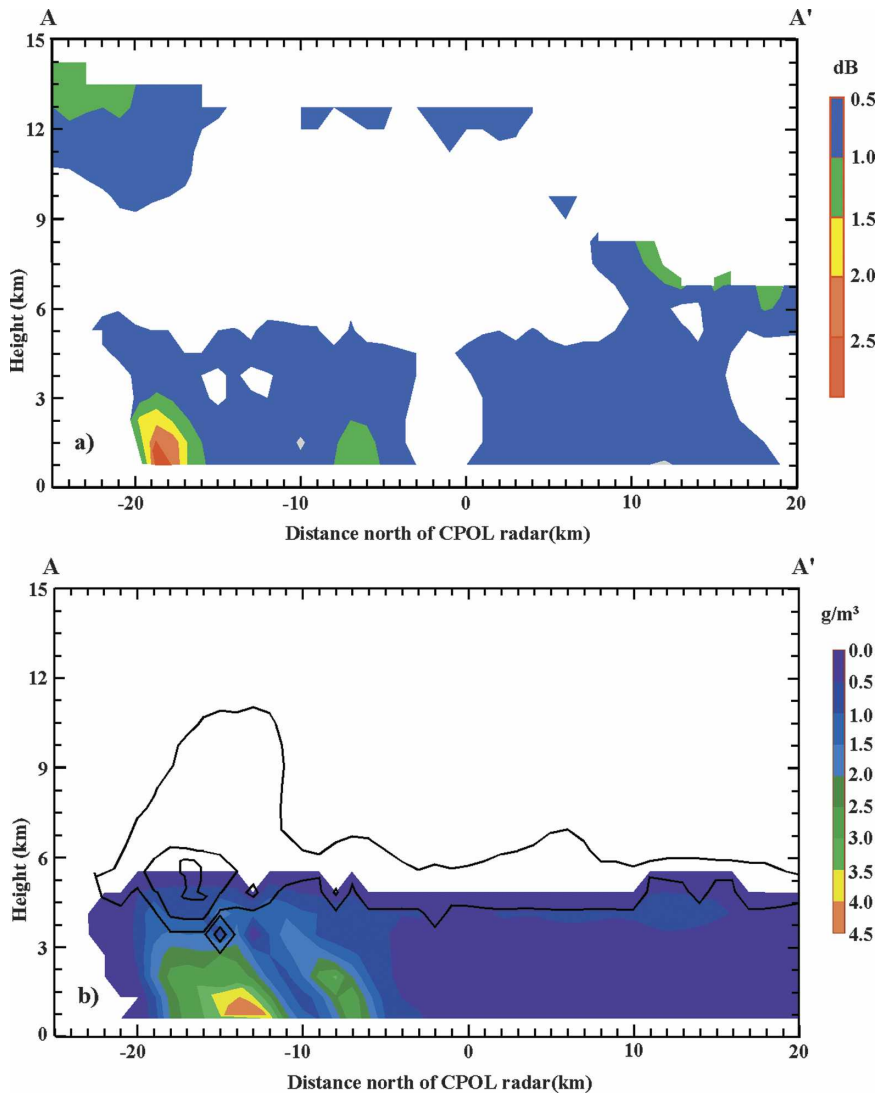

FIG. 8. Same as in Fig. 6, but for (a) differential reflectivity (dB), and (b) hydrometeor density: rainwater (g m^{-3}) (shaded) and ice water (contoured at 0.1, 0.5, and 1.0 g m^{-3}) retrieved from radar reflectivity and polarimetric parameters.

show erect vertical convection and an anvil cloud that elongates northward with the meridional length of about 60 km. The differences between the simulation and observation are that the modeled density maximum occurs in the midtroposphere whereas the observed maximum appears near the surface. In addition, the magnitude of modeled density is larger than observed density, in particular, the magnitude of ice density. The overestimation of ice density is likely attributed to the overestimation of vertical velocity, particularly at midlevels in the mixed phase zone, in the convective core by the two-dimensional model (cf. Figs. 7 and 6).

Although the above comparison between the simulation and observation shows similarity, the analysis of individual clouds and associated circulation in the 2D framework may have limitations. For example, Moncrieff and Miller (1976) found that the 3D framework is necessary to simulate the 3D crossover flow pattern associated with propagating tropical squall lines. Thus, caution should be exercised when the following 2D results are applied.

4. Surface rainfall and cloud microphysical processes

Figure 10a shows the temporal evolution of the meridional distribution of the surface rain rate in a se-

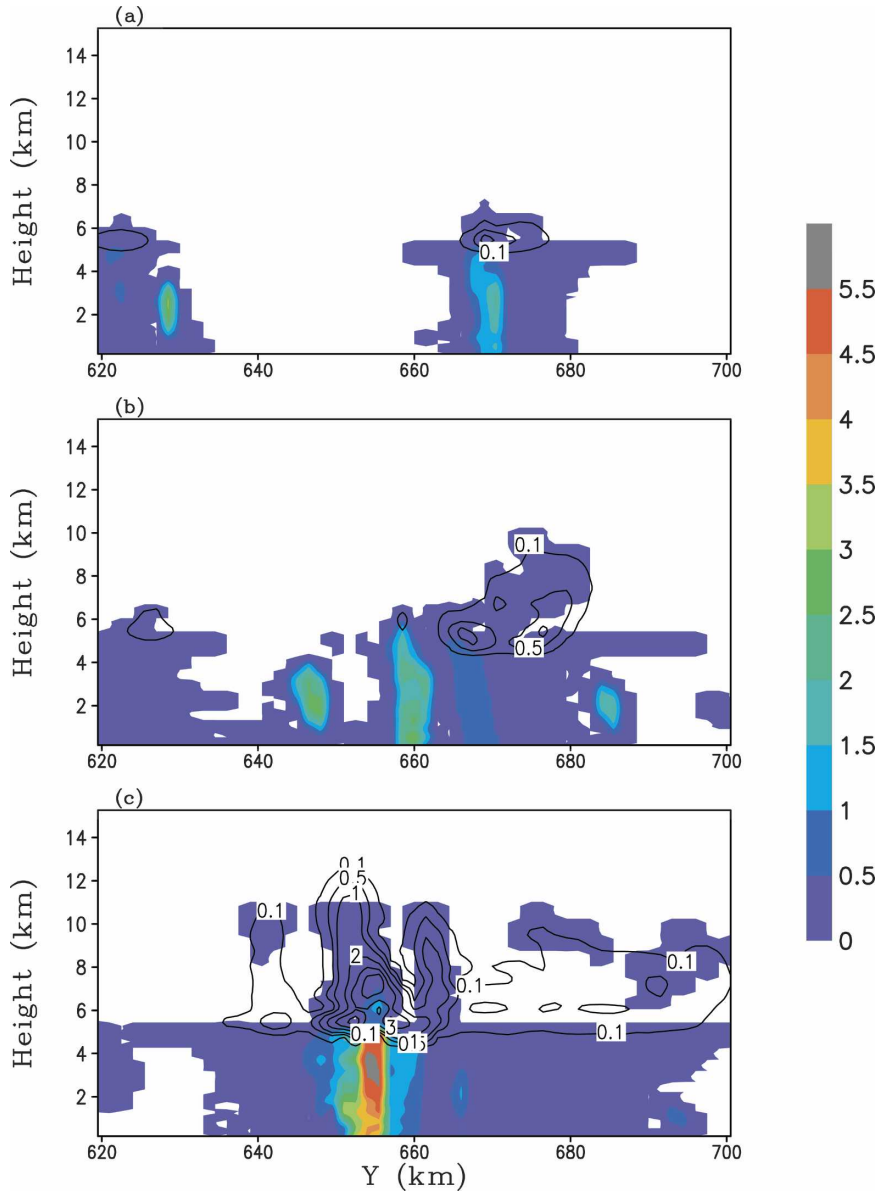

FIG. 9. Model-derived meridional–vertical (y–z) cross sections of hydrometeor density: rainwater (g m^{-3}) (shaded) and ice water (contoured at 0.1, 0.5, 1, 2, 3, and 4 g m^{-3}) at (a) 0700, (b) 0800, and (c) 0900 LST 20 May 1998.

lected time and domain. A major rainband initiates around 670 km after hour 5, barely moves and intensifies quickly, reaching up to 21.9 mm h^{-1} at hour 7 (also see Table 2). The rainband weakens quickly after hour 8 and it maintains light rain until hour 13. Meanwhile, new rainbands form around 660, 653, 647, and 640 km at hours 7, 8, 9, and 10, respectively. Thus, rainbands propagate southward while the individual rainband barely moves.

To examine the physical processes including moisture and cloud budget that are responsible for the surface rainfall variation, the major terms in the surface rainfall equation derived by Gao et al. (2005b) will be analyzed in the following discussions. The surface rain rate is contributed by the local vapor change (Q_{WVT}), vapor convergence (Q_{WVF}), surface evaporation (Q_{WVE}), and cloud source/sink (Q_{CM}). And, the surface rainfall equation can be expressed by

$$P_s = Q_{\mathrm{WVT}} + Q_{\mathrm{WVF}} + Q_{\mathrm{WVE}} + Q_{\mathrm{CM}}, \qquad (8)$$

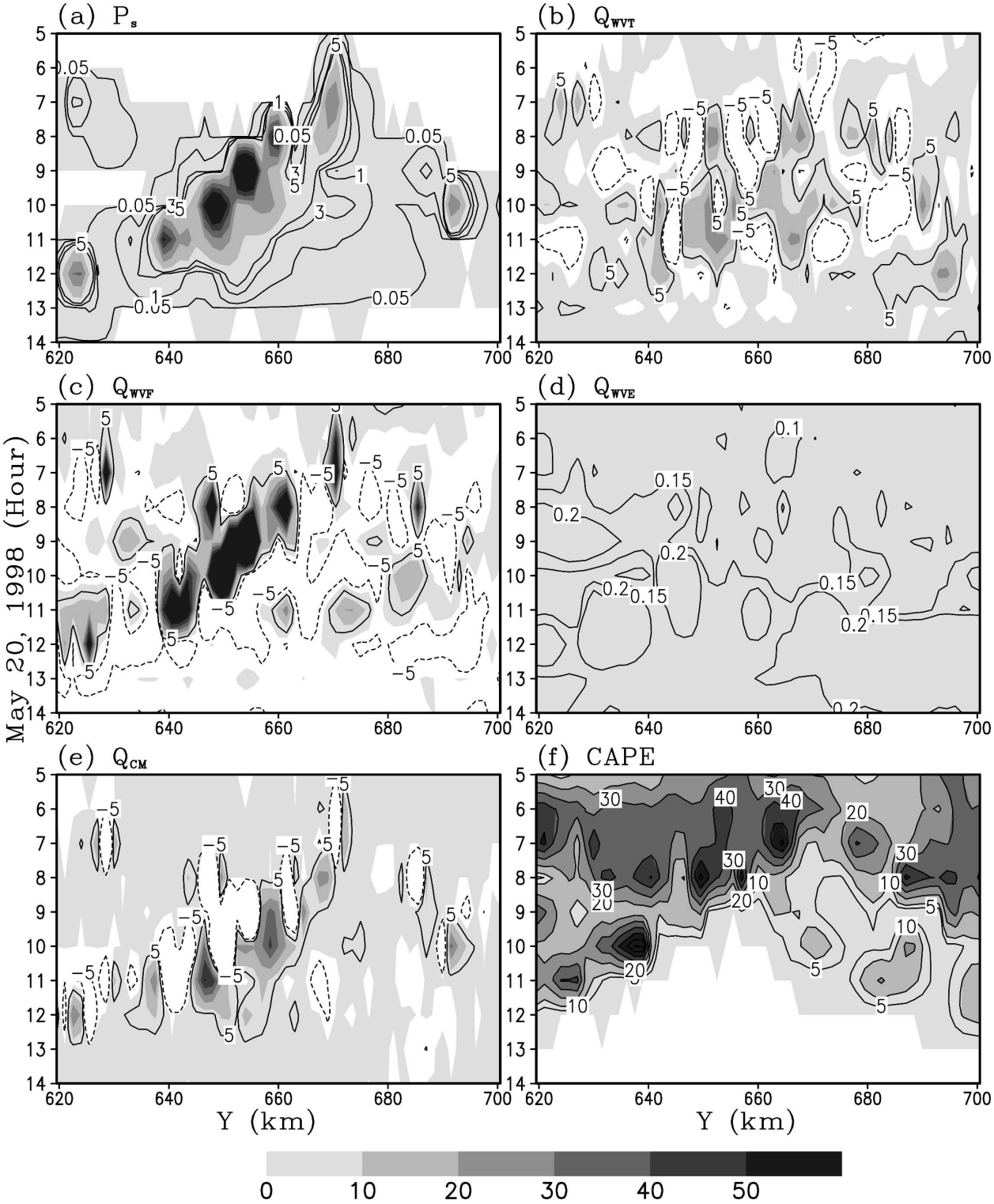

FIG. 10. Temporal and horizontal distribution of (a) P_S, (b) Q_{WVT}, (c) Q_{WVF}, (d) Q_{WVE}, (e) Q_{CM}, and (f) CAPE on 20 May 1998. Contour intervals are 0.05, 1, 3, and 5 mm h^{-1} for P_S; 5 and 5 mm h^{-1} for Q_{WVT}, Q_{WVF}, and Q_{CM}; 0.05, 0.1, 0.15, and 0.2 mm h^{-1} for Q_{WVE}; and 5, 10, 20, 30, 40, 50, and 60 × 10 J kg^{-1} for CAPE. The units are mm h^{-1} for P_S, Q_{WVT}, Q_{WVF}, Q_{WVE}, Q_{CM}, and 10 J kg^{-1} for CAPE.

TABLE 2. The P_S, Q_{WVT}, Q_{WVF}, Q_{WVE}, and Q_{CM} (mm h^{-1}) along a life span of convection averaged in 669–672 km from 0500 to 0900 LST 19 May 1998.

Stage	Case	LST	P_S	Q_{WVT}	Q_{WVF}	Q_{WVE}	Q_{CM}
Preformation	A	0500	0	−2.6	2.4	0.2	0
Formation	B	0600	6.7	−2.3	16.0	0.2	−7.2
Mature	C	0700	21.9	−7.2	30.8	0.2	−1.9
Weakening	D	0800	12.1	11.7	−11.8	0.2	12.0
Dissipating	E	0900	0.2	2.8	−4.5	0.2	1.7

where

$$Q_{WVT} = -\frac{\partial[q_v]}{\partial t};$$

$$Q_{WVF} = -\left[\overline{u}^{o}\frac{\partial \overline{q}_v}{\partial x}\right] - \left[\overline{w}^{o}\frac{\partial \overline{q}_v}{\partial z}\right] - \left[\frac{\partial(u'q_v')}{\partial x}\right] - \left[\overline{u}^{o}\frac{\partial q_v'}{\partial x}\right] - \left[\overline{w}^{o}\frac{\partial q_v'}{\partial z}\right] - \left[w'\frac{\partial \overline{q}_v}{\partial z}\right];$$

$$Q_{WVE} = E_s;$$

$$Q_{CM} = -\frac{\partial[q_5]}{\partial t} - \left[\frac{\partial(uq_5)}{\partial x}\right];$$

where q_v is the specific humidity; u and w are zonal and vertical wind components, respectively; E_S is the surface evaporation rate; $q_5 = q_c + q_r + q_i + q_s + q_g$, q_c, q_r, q_i, q_s, q_g are the mixing ratios of cloud water (small cloud droplets), raindrops, cloud ice (small ice crystals), snow (density 0.1 g cm^{-3}), and graupel (density 0.4 g cm^{-3}), respectively; the overbar denotes a zonal mean; the prime is a perturbation from zonal mean; [·] is a mass integration; and superscript o is an imposed observed value. Positive values of Q_{WVT}, Q_{WVF}, and Q_{CM} denote local vapor loss (atmospheric drying), vapor convergence, and local hydrometeor loss/hydrometeor convergence, respectively, whereas negative Q_{WVT}, Q_{WVF}, and Q_{CM} denote local vapor gain (atmospheric moistening), vapor divergence, and local hydrometeor gain/hydrometeor divergence, respectively. Since the surface rainfall equation is derived from atmospheric moisture and cloud budgets, the local vapor loss and vapor convergence contribute to the surface rainfall through condensation and deposition and other microphysical processes.

Figures 10b–f show temporal evolution of meridional distribution of each term in the right-hand side of Eq. (8), and convective available potential energy (CAPE) for the reversible moist adiabatic process (Li et al. 2002b), respectively. The surface rain rate is contributed by the local vapor change, vapor convergence, and the local cloud change/hydrometeor convergence whereas the surface evaporation flux is much smaller than the other rainfall processes and negligible. The surface rainfall is always located to the north of large amounts of the CAPE and the CAPE becomes small after the passage of rainbands (Fig. 10f), indicating the release of unstable energy for the development of convection. Due to similar life cycles for individual rainbands, the rainband around 670 km from hours 5 to 9 will be analyzed.

In general, the convection will be analyzed in terms of circulation (Fig. 11, and wind vectors in Fig. 7), vertical thermal (Fig. 12), and vertical vapor (Fig. 13) structures, as well as the cloud microphysical budget (Fig. 14). A summary of the areas of analysis, the rain rate, and values of each term in the surface rainfall equation at different stages of the convection is given in Table 2. The data are averaged near the action centers. It should be emphasized that although different averaging areas may change the values of surface rainfall equations in Table 2, contributions of dominant terms to surface rainfall will not be changed. The surface rainfall budget averaged over the target rainband during its preformation stage at 0500 LST (Fig. 11a; case A in Table 2), shows that local vapor change (Q_{WVT} = −2.6 mm h^{-1}) and vapor convergence (Q_{WVF} = 2.4 mm h^{-1}) nearly cancel each other out. Thus, without any hydrometeor convergence (Q_{CM} = 0 mm h^{-1}), surface rainfall as well as clouds does not occur. Although there is vapor convergence, it only moistens the atmosphere. The southerly winds appear in the lower troposphere whereas the northerly winds occur in the upper troposphere (Fig. 11a). The negative temperature (Fig. 12a) and positive vapor (Fig. 13a) perturbations also appear in the lower troposphere.

The surface rainfall budget averaged over the target rainband during its formation stage at 0600 LST (Fig. 11b; case B in Table 2), reveals that rain rate (P_s = 6.7 mm h^{-1}) is mainly determined by vapor convergence (Q_{WVF} = 16.0 mm h^{-1}) and hydrometeor convergence (Q_{CM} = −7.2 mm h^{-1}). Thus, the vapor convergence plays a major role to enhance both surface rainfall and hydrometeors. The hydrometeors (Fig. 11b) occupy a narrow meridional area and show an erect vertical structure with the extension of 4 km. The ascending

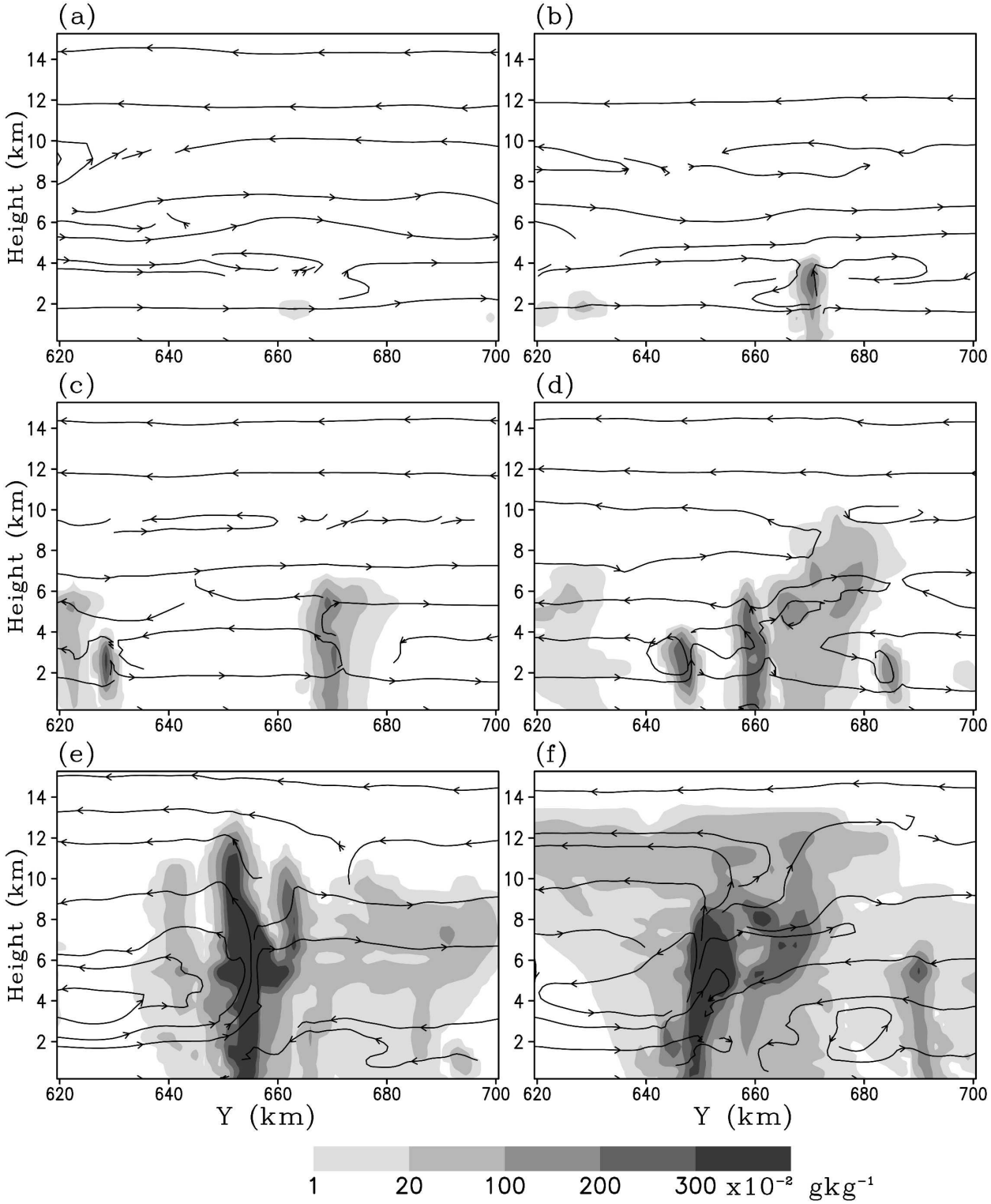

FIG. 11. Meridional–vertical (y–z) cross sections of streamlines and sum of the mixing ratios of hydrometeors (background shading) from 0500 to 1000 LST 20 May 1998 in 1-h intervals.

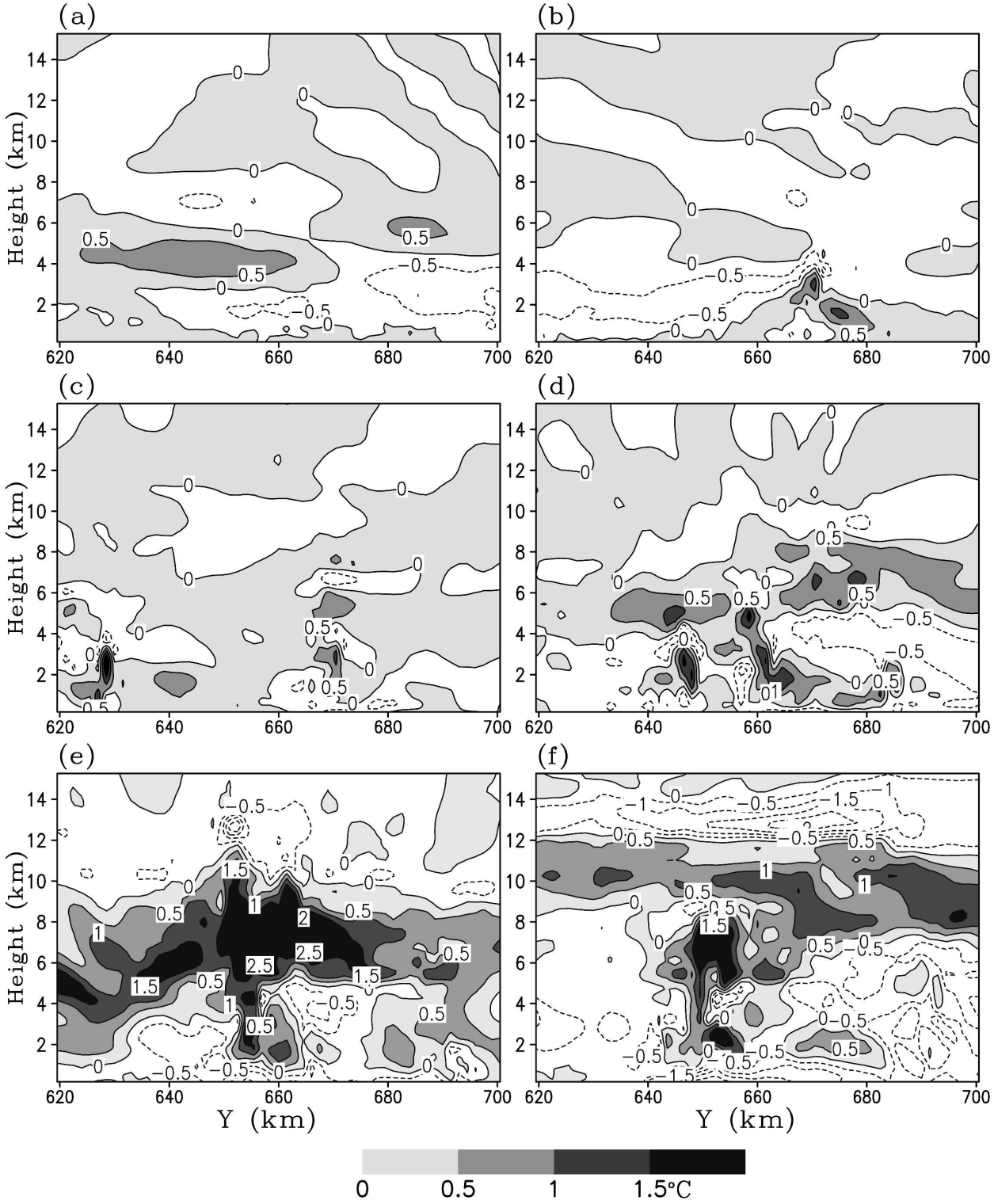

FIG. 12. Meridional–vertical (y–z) cross sections of temperature anomaly (°C) from the meridional mean from 0500 to 1000 LST 20 May 1998 in 1-h intervals.

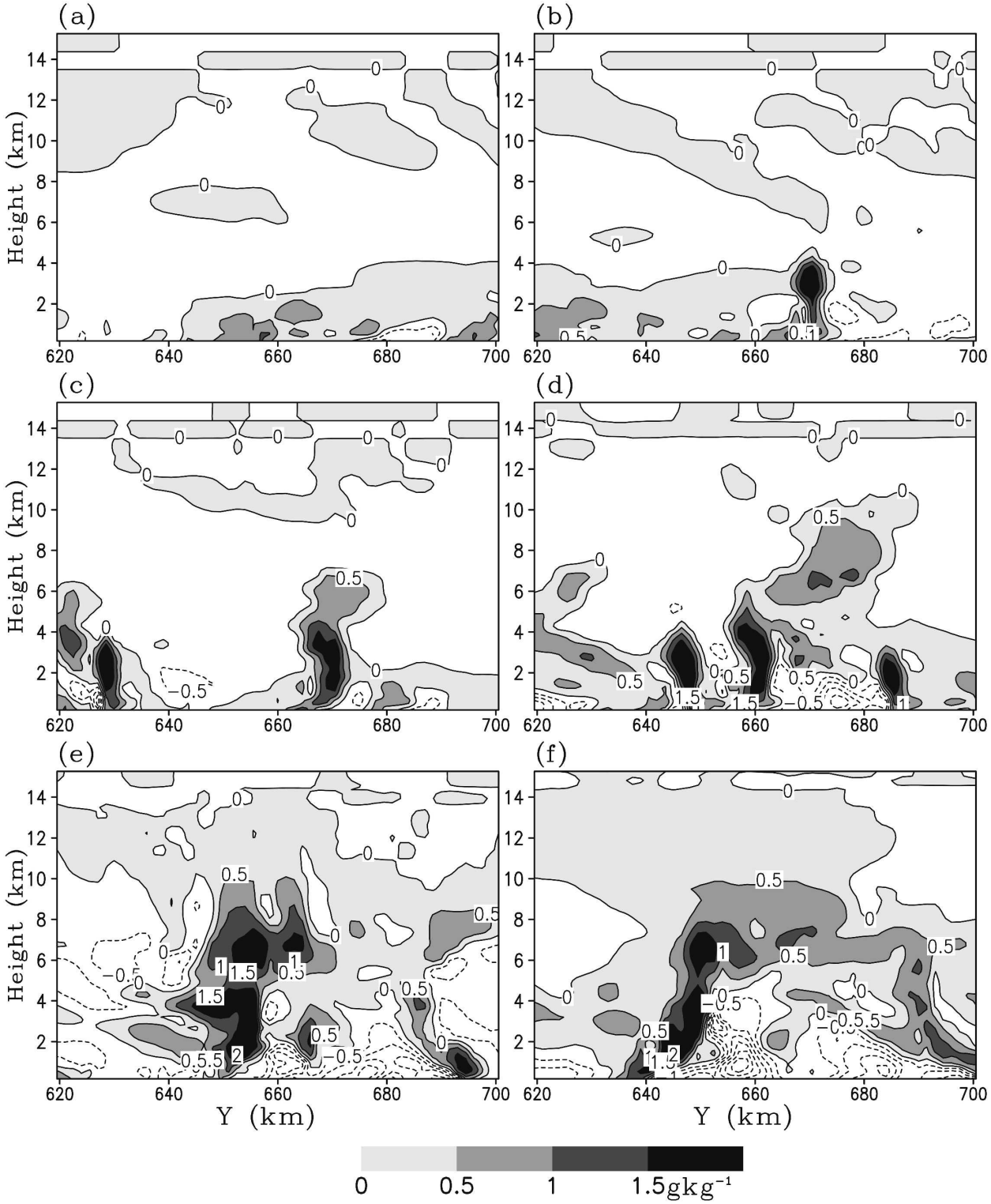

FIG. 13. Same as in Fig. 12 except for the specific humidity anomaly (g kg^{-1}).

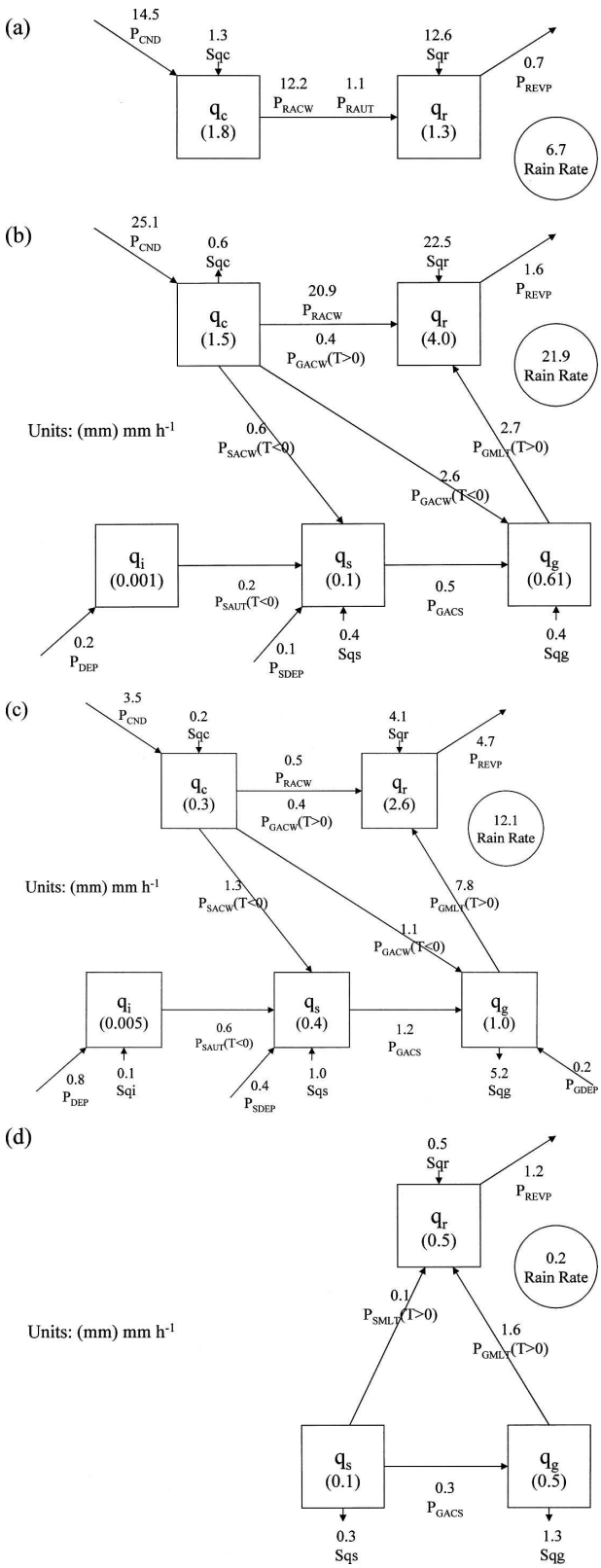

FIG. 14. Cloud microphysical budgets averaged in 669–672 km from 0600 to 0900 LST 20 May 1998 in 1-h intervals. Units for hydrometeors and conversions are mm and mm h^{-1}, respectively.

motion associated with the convective center results from a strong convergence. The positive temperature (Fig. 12b) and vapor (Fig. 13b) perturbations are associated with the maximum hydrometeors. Since cloud hydrometeors occur below 4 km (warmer than 0°C), only water hydrometeors appear with the liquid water path (LWP; $[q_c] + [q_r] = 3.1$ mm; Fig. 14a). Most of vapor condensation ($[P_{\mathrm{CND}}] = 14.5$ mm h^{-1}) goes to raindrops through the collection of cloud water by raindrops ($[P_{\mathrm{RACW}}] = 12.2$ mm h^{-1}). The sum of rain microphysics ($[S_{\mathrm{qr}}] = 12.6$ mm h^{-1}) is larger than surface rain rate (6.7 mm h^{-1}), suggesting that part of the rain moves horizontally to the neighboring area.

The surface rainfall budget averaged over the target rainband during its mature phase at 0700 LST (Fig. 11c; case C in Table 1), shows that the rain rate ($P_s = 21.9$ mm h^{-1}) is mainly determined by vapor convergence ($Q_{\mathrm{WVF}} = 30.8$ mm h^{-1}) and local vapor change ($Q_{\mathrm{WVT}} = -7.2$ mm h^{-1}). Thus, the vapor convergence is the only source that is responsible for the surface rainfall. The cloud hydrometeors (Fig. 11c) occupy a relatively large meridional area compared to case B. The strong updraft causes the vertical extension of clouds to 6 km. The positive temperature (Fig. 12c) and vapor (Fig. 13c) perturbations are collocated with the maximum cloud hydrometeors. The LWP ($[q_c] + [q_r] = 5.5$ mm) is larger than the ice water path (IWP; $[q_i] + [q_s] + [q] = 0.7$ mm; Fig. 14b). This suggests the dominance of water hydrometeors in the convective system. The four fifths of vapor condensation ($[P_{\mathrm{CND}}] = 25.1$ mm h^{-1}) goes to raindrops though the collection of cloud water by raindrops ($[P_{\mathrm{RACW}}] = 20.9$ mm h^{-1}). Meanwhile, less than one-fifth of vapor condensation supports precipitation ice through the accretion of cloud water by precipitation ice ($[P_{\mathrm{SACW}}] + [P_{\mathrm{GACW}}] = 3.3$ mm h^{-1}). With a small vapor deposition rate ($[P_{\mathrm{CND}}] + [P_{\mathrm{SDEP}}] + [P_{\mathrm{GDEP}}] = 0.3$ mm h^{-1}), the melting of precipitation ice to raindrops ($[P_{\mathrm{GMLT}}] = 2.7$ mm h^{-1}) plays a minor role in determining the surface rain rate. Similar values of P_s (21.9 mm h^{-1}) and $[S_{\mathrm{qr}}]$ (22.5 mm h^{-1}) suggest that surface rainfall is mainly generated by cloud microphysical processes. These results are also consistent with the C-POL observations (Fig. 8).

In the surface rainfall budget averaged over the target rainband during its weakening stage at 0800 LST (Fig. 11d; case D in Table 2), the rain rate ($P_s = 12.1$ mm h^{-1}) is determined by local vapor change ($Q_{\mathrm{WVT}} = 11.7$ mm h^{-1}), vapor convergence ($Q_{\mathrm{WVF}} = -11.8$ mm h^{-1}), and hydrometeor convergence ($Q_{\mathrm{CM}} = 12.0$ mm h^{-1}). Thus, the local vapor and hydrometeor loss overcome the vapor divergence to support the surface rainfall. Unlike previous discussed situations, the cloud (Fig. 11d) shows a loose structure with the vertical ex-

tension to 10 km. Weak updraft appears in the midtroposphere while strong downdraft occurs in the lower troposphere, which leads to the vapor divergence. The vapor divergence is associated with vapor convergence in the neighboring areas where new clouds form. The positive temperature (Fig. 12d) and vapor (Fig. 13d) perturbations occur around the hydrometeor center in the midtroposphere. Here $P_s - [S_{qr}]$ (8.0 mm h^{-1}) is twice as large as $[S_{qr}]$ (4.1 mm h^{-1}) (Fig. 14c), indicating that a large amount of surface rainfall come from the local hydrometeor loss or hydrometeor convergence and that cloud microphysics plays a minor role in determining the surface rain rate. Three aspects should be noticed in the cloud microphysical budget. First, the LWP ($[q_c] + [q_r] = 2.9$ mm) is twice as large as the IWP ($[q_i] + [q_s] + [q_g] = 1.5$ mm). Second, less than one-third of vapor condensation ($[P_{CND}] = 3.5$ mm h^{-1}) goes to raindrops though the collection and accretion of cloud water by raindrops ($[P_{RACW}] + [P_{GACW}] = 0.9$ mm h^{-1}), whereas the two thirds support precipitation ice through the accretion of cloud water by precipitation ice ($[P_{SACW}] + [P_{GACW}] = 2.4$ mm h^{-1}). Third, large graupel loss ($[S_{qg}] = -5.2$ mm h^{-1}) along with the accretion of cloud water ($[P_{GACW}] = 1.1$ mm h^{-1}) and snow ($[P_{GACS}] = 1.2$ mm h^{-1}) by graupel lead to the melting of precipitation ice to raindrops ($[P_{GMLT}] = 7.8$ mm h^{-1}), which is a major process in raindrop budget.

In the surface rainfall budget averaged over the target rainband during its dissipating stage at 0900 LST (Fig. 11f; case E in Table 2), when the convection was at the stage of dissipation, the rain rate ($P_s = 0.2$ mm h^{-1}) is small because of a large cancellation among local vapor change ($Q_{WVT} = 2.8$ mm h^{-1}), vapor convergence ($Q_{WVF} = -4.5$ mm h^{-1}), and hydrometeor convergence ($Q_{CM} = 1.7$ mm h^{-1}). The cloud shows a large hydrometeor mixing ratio around 5.5 km, and an updraft disappears in the lower troposphere (Fig. 11f), indicating an anvil cloud and stratiform rain during the late stages of the convective system. The negative temperature (Fig. 12f) and positive vapor (Fig. 13f) perturbations occur in the mid- and lower troposphere. Four aspects should be noticed in the cloud microphysical budget (Fig. 14d). First, cloud water and ice disappear due to a lack of vapor condensation and deposition. Second, the IWP ($[q_s] + [q_g] = 0.6$ mm) is larger than the LWP ($[q_r] = 0.5$ mm). Third, the major source for raindrops is the melting of precipitation ice to raindrops ($[P_{GMLT}] = 1.6$ mm h^{-1}). Fourth, $[S_{qr}]$ is 0.5 mm h^{-1} whereas P_s is 0.2 mm h^{-1}. This implies that the anvil microphysics play an important role in determining light rainfall.

5. Summary

A case study of the monsoon convection observed during the South China Sea Monsoon Experiment (SCSMEX) is performed with a two-dimensional cloud-resolving simulation combined with dual-Doppler/polarimetric radar analysis to investigate the evolution, structure of the system along with the cloud microphysical and surface rainfall processes. The model is forced by the large-scale vertical velocity, zonal wind, and horizontal advections observed and derived from SCSMEX data. The comparison between the simulations and observations and the analysis of the surface rainfall and cloud microphysical processes are conducted with the hourly data on 20 May 1998. In general, the cloud-resolving model did a reasonable job simulating the evolution and structure of the convection observed during the SCS monsoon onset. Both the radar observations and model simulations show the following: 1) the positions of the convection are relatively stable with little movement throughout its life cycle, 2) the reflectivity pattern is straight upward with rapid reduction with height above the melting layer, 3) the center of the updraft is collocated with the convective core, and a transition zone generated by convective downward motion follows, and 4) the convective cold pool is weak, resulting in a wider updraft zone. However, due to the limitation of the two-dimensional model, the simulations also have significant departure from the observations. The model displays an overestimated maximum of updraft of 10 m s^{-1}, comparing to 5–6 m s^{-1} normally observed in tropical oceanic convection. The overestimation, especially at the midlevels, also directly influences the model simulated maximum reflectivity at an elevated altitude (5–8 km), comparing to below 3 km observed by the radar network.

The surface rainfall processes and associated thermodynamic, dynamic, and cloud microphysical processes are examined in terms of surface rainfall, temperature and moisture perturbations, circulations, and the cloud microphysical budget. Before clouds and surface rainfall occur, vapor convergence enhances local moisture. Vapor convergence quickly intensities to act as the major contributor to the surface rainfall processes and the cloud development as hydrometeors and updrafts show an erect vertical structure. The cloud microphysical budget associated with a large surface rainfall shows the dominance of water microphysical processes that determine the surface rain rate, in which the large vapor condensation causes a large amount of raindrops for the precipitation through the collection of cloud water by raindrops. On the other hand, riming/graupel makes small contribution to surface rainfall up to and includ-

ing the mature stage. This is also verified by the C-POL radar observations. During the weakening of the convective system, the ice microphysical processes become dominant as the vapor divergence associated with the lower-tropospheric subsidence prevails. Local vapor loss is a major player in the surface rainfall.

Acknowledgments. The authors would like to acknowledge those who participated in SCSMEX, especially T. Rickenbach (NASA GSFC), R. Cifelli (Colorado State University), P. Kucera (University of Iowa), T. Keenan (BMRC, Australia), and J. Gerlach (NASA WSFC) for their involvement in the radar observations and preliminary data processing. Thanks also go to R. Adler, W.-K. Tao (NASA GSFC), and R. Johnson and S. Rutledge (Colorado State University) for many stimulating discussions about the tropical convection. This research was sponsored by the National Aeronautics and Space Administration (NASA) under TRMM Grants NAG5-9699.

REFERENCES

Bringi, V. N., and V. Chandrasekar, 2001: *Polarimetric Doppler Weather Radar: Principles and Applications*. Cambridge University Press, 636 pp.

Carey, L. D., and S. A. Rutledge, 2000: The relationship between precipitation and lightening in tropical island convection: A C-band polarimetric radar study. *Mon. Wea. Rev.,* **128,** 2687–2710.

Chan, J. C. L., Y. Wang, and J. Xu, 2000: Dynamic and thermodynamic characteristics associated with the onset of the 1998 South China Sea summer monsoon. *J. Meteor. Soc. Japan,* **78,** 367–380.

Chou, M.-D., and M. J. Suarez, 1994: An efficient thermal infrared radiation parameterization for use in general circulation models. NASA Tech. Memo. 104606, Vol. 3, 85 pp. [Available from NASA/Goddard Space Flight Center, Code 913, Greenbelt, MD 20771.]

——, D. P. Kratz, and W. Ridgway, 1991: Infrared radiation parameterization in numerical climate models. *J. Climate,* **4,** 424–437.

——, M. J. Suarez, C.-H. Ho, M. M.-H. Yan, and K.-T. Lee, 1998: Parameterizations for cloud overlapping and shortwave single scattering properties for use in general circulation and cloud ensemble models. *J. Atmos. Sci.,* **55,** 201–214.

Cifelli, R., W. A. Peterson, L. D. Carey, and S. A. Rutledge, 2002: Radar observation of the kinematic, microphysical, and precipitation characteristics of two MCSs in TRMM-LBA. *J. Geophys. Res.,* **107,** 8077, doi:10.1029/2000JD000264.

Ding, Y., and Y. Liu, 2001: Onset and the evolution of the summer monsoon over the South China Sea during SCSMEX field experiment in 1998. *J. Meteor. Soc. Japan,* **79,** 255–276.

Gao, S., F. Ping, X. Li, and W.-K. Tao, 2004: A convective vorticity vector associated with tropical convection: A 2D cloud-resolving modeling study. *J. Geophys. Res.,* **109,** D14106, doi:10.1029/2004JD004807.

——, ——, and ——, 2005a: Cloud microphysical processes associated with the diurnal variations of tropical convection: A 2D cloud resolving modeling study. *Meteor. Atmos. Phys.,* **91,** 9–16.

——, X. Cui, Y. Zhu, and X. Li, 2005b: Surface rainfall processes as simulated in a cloud resolving model. *J. Geophys. Res.,* **110,** D10202, doi:10.1029/2004JD005467.

Golestani, Y., V. Chandrasekar, and V. N. Bringi, 1989: Intercomparison of multiparameter radar measurements. Preprints, *24th Int. Conf. on Radar Meteorology,* Boston, MA, Amer. Meteor. Soc., 309–314.

Grabowski, W. W., X. Wu, and M. W. Moncrieff, 1996: Cloud-resolving model of tropical cloud systems during Phase III of GATE. Part I: Two-dimensional experiments. *J. Atmos. Sci.,* **53,** 3684–3709.

Houze, R. A., Jr., 1977: Structure and dynamics of a tropical squall-line system. *Mon. Wea. Rev.,* **105,** 1540–1567.

Johnson, R. H., and P. E. Ciesielski, 2002: Characteristics of the 1998 summer monsoon onset over the northern South China Sea. *J. Meteor. Soc. Japan,* **80,** 561–578.

——, S. L. Aves, P. E. Ciesielski, and T. D. Keenan, 2005: Organization of oceanic convection during the onset of the 1998 East Asian summer monsoon. *Mon. Wea. Rev.,* **133,** 131–148.

Jorgensen, D. P., and M. A. LeMone, 1989: Vertical velocity characteristics of oceanic convection. *J. Atmos. Sci.,* **46,** 621–640.

——, ——, and S. B. Trier, 1997: Structure and evolution of the 22 February 1993 TOGA COARE squall line: Aircraft observations of precipitation, circulation, and surface energy fluxes. *J. Atmos. Sci.,* **54,** 1961–1985.

Krueger, S. K., Q. Fu, K. N. Liou, and H.-N. S. Chin, 1995: Improvement of an ice-phase microphysics parameterization for use in numerical simulations of tropical convection. *J. Appl. Meteor.,* **34,** 281–287.

Lau, K.-M., and Coauthors, 2000: Report of the field operations and early results of the South China Sea Monsoon Experiment (SCSMEX). *Bull. Amer. Meteor. Soc.,* **81,** 1261–1270.

——, X. Li, and H.-T. Wu, 2002: Evolution of the large scale circulation, cloud structure and regional water cycle associated with the South China Sea monsoon during May–June, 1998. *J. Meteor. Soc. Japan,* **80,** 1129–1147.

Li, X., C.-H. Sui, K.-M. Lau, and M.-D. Chou, 1999: Large-scale forcing and cloud–radiation interaction in the tropical deep convective regime. *J. Atmos. Sci.,* **56,** 3028–3042.

——, ——, and ——, 2002a: Dominant cloud microphysical processes in a tropical oceanic convective system: A 2-D cloud resolving modeling study. *Mon. Wea. Rev.,* **130,** 2481–2491.

——, ——, and ——, 2002b: Interactions between tropical convection and its environment: An energetics analysis of a 2-D cloud resolving simulation. *J. Atmos. Sci.,* **59,** 1712–1722.

Lin, Y.-L., R. D. Farley, and H. D. Orville, 1983: Bulk parameterization of the snow field in a cloud model. *J. Climate Appl. Meteor.,* **22,** 1065–1092.

Moncrieff, M. W., and M. J. Miller, 1976: The dynamics and simulation of tropical cumulonimbus and squall line. *Quart. J. Roy. Meteor. Soc.,* **102,** 373–394.

Rutledge, S. A., and P. V. Hobbs, 1983: The mesoscale and microscale structure and organization of clouds and precipitation in mid-latitude cyclones. Part VIII: A model for the "seeder-feeder" process in warm-frontal rainbands. *J. Atmos. Sci.,* **40,** 1185–1206.

——, and ——, 1984: The mesoscale and microscale structure and organization of clouds and precipitation in mid-latitude cyclones. Part XII: A diagnostic modeling study of precipitation development in narrow cold-frontal rainbands. *J. Atmos. Sci.,* **41,** 2949–2972.

Simpson, J., Ed., 1988: TRMM: A satellite mission to measure tropical rainfall, report of the science steering group. National Aeronautics and Space Administration, Goddard Space Flight Center, 94 pp.

Soong, S. T., and Y. Ogura, 1980: Response of trade wind cumuli to large-scale processes. *J. Atmos. Sci.,* **37,** 2035–2050.

——, and W. K. Tao, 1980: Response of deep tropical cumulus clouds to mesoscale processes. *J. Atmos. Sci.,* **37,** 2016–2034.

Sui, C.-H., K.-M. Lau, W.-K. Tao, and J. Simpson, 1994: The tropical water and energy cycles in a cumulus ensemble model. Part I: Equilibrium climate. *J. Atmos. Sci.,* **51,** 711–728.

——, X. Li, and K.-M. Lau, 1998: Radiative-convective processes in simulated diurnal variations of tropical oceanic convection. *J. Atmos. Sci.,* **55,** 2345–2359.

Tao, S., and L. Chen, 1987: A review of recent research on the East Asian summer monsoon in China. *Monsoon Meteorology,* C.-P. Chang and T. N. Krishnamurti, Eds., Oxford University Press, 60–92.

Tao, W.-K., and J. Simpson, 1993: The Goddard Cumulus Ensemble model. Part I: Model description. *Terr. Atmos. Oceanic Sci.,* **4,** 35–72.

——, ——, and M. McCumber, 1989: An ice-water saturation adjustment. *Mon. Wea. Rev.,* **117,** 231–235.

——, C.-L. Shie, J. Simpson, S. Braun, R. H. Johnson, and P. E. Ciesielski, 2003: Convective systems over the South China Sea: Cloud-resolving model simulations. *J. Atmos. Sci.,* **60,** 2929–2956.

Wang, J.-J., 2004: Evolution and structure of the mesoscale convection and its environment: A case study during the early onset of the Southeast Asian summer monsoon. *Mon. Wea. Rev.,* **132,** 1104–1120.

——, and L. Carey, 2005: Structure and evolution of an oceanic squall line during the South China Sea Monsoon Experiment. *Mon. Wea. Rev.,* **133,** 1544–1561.

Wentz, F. J., C. Gentemann, D. Smith, and D. Chelton, 2000: Satellite measurements of sea surface temperature through clouds. *Science,* **288,** 847–850.

Wu, X., W. W. Grabowski, and M. W. Moncrieff, 1998: Long-term evolution of cloud systems in TOGA COARE and their interactions with radiative and surface processes. Part I: Two-dimensional cloud-resolving model. *J. Atmos. Sci.,* **55,** 2693–2714.

Xu, K.-M., and D. A. Randall, 1996: Explicit simulation of cumulus ensembles with the GATE Phase III data: Comparison with observations. *J. Atmos. Sci.,* **53,** 3710–3736.

Zipser, E. J., and M. A. LeMone, 1980: Cumulonimbus vertical velocity events in GATE. Part II: Synthesis and model core structure. *J. Atmos. Sci.,* **37,** 2458–2469.